# Flexible perovskite photovoltaic modules and cells rased on atomic layer deposited compact layers and UV-irradiated TiO2 scaffolds on plastic substrates

# Flexible Perovskite Photovoltaic Modules and Solar Cells Based on Atomic Layer Deposited Compact Layers and UV-Irradiated $TiO_2$ Scaffolds on Plastic Substrates

*Francesco Di Giacomo, Valerio Zardetto, Alessandra D'Epifanio, Sara Pescetelli, Fabio Matteocci, Stefano Razza, Aldo Di Carlo, Silvia Licoccia, Wilhelmus M. M. Kessels, Mariadriana Creatore, and Thomas M. Brown**

Recently, research on hybrid organometal halide perovskites for photovoltaic applications has delivered impressive growth in power conversion efficiencies (PCEs) with a current certified record of 17.9% and growing.[1–6] Key advantages of perovskites devices, together with high PCEs, are represented by the ease of the solution processing steps and their low temperature (<140 °C).[7,8] These values enable the fabrication on plastic substrates,[9] compatible with a continuous roll-to-roll manufacturing which can potentially contribute to dramatically lower the production costs of large area modules.[10] Moreover, flexible devices can also be conformed to curved surfaces to enhance power conversion densities.[11,12] We have found only a handful of reports on flexible perovskite solar cells, four based on planar scaffold-less *p–i–n* architectures with PCEs of up to 10.2%,[7,13–15] and one based on a ZnO nanorod scaffold (with a lower efficiency, of 2%).[16] However, architectures with a mesostructured $TiO_2$ or $Al_2O_3$ scaffold have typically shown superior efficiency and stability on glass substrates.[6,17–20] Whereas the $Al_2O_3$ layer may not require particularly careful annealing since no charge injection occurs into that oxide,[21] the development of large-area low-temperature material formulations and processes for yielding high quality compact hole blocking layers (usually applied by high temperature spray pyrolysis) and well-connected mesoporous nanocrystalline $TiO_2$ (typical oven treatment at 450–500 °C), applicable to plastic substrates is urgent.[22] Recently, we proposed a UV irradiation process on a customized $TiO_2$ nanoparticle paste for the fabrication of efficient flexible dye sensitized solar cells (DSCs).[23] In this work, we demonstrate how UV irradiation can be successfully employed for developing the very thin $TiO_2$ mesoporous scaffold in this new type of plastic perovskite solar devices. The electron collecting compact layer is also essential for delivering performing devices as it lowers the carrier recombination probability at the interface between the transparent conductive oxide (TCO) and perovskite layers. The only material utilized on plastic substrates up to now has been ZnO deposited by electrodeposition and spin coating of nanoparticles dispersion.[12,16] Atomic layer deposition (ALD) has been used for the fabrication of ultrathin, uniform, and conformal layers in several PV technologies.[24] Thermal ALD was adopted to produce a compact $TiO_2$ layer on glass perovskite cells, yielding higher device PCE compared to spray pyrolysis or the spin coating of a sol-gel solution.[25,26] Recently, we explored the benefit of using plasma assisted ALD applied to flexible DSCs.[27] Here we adopt plasma ALD of cyclopentadienyl alkylamido titanium $Ti(CpMe)(NMe_2)_3$ precursor to obtain an effective compact $TiO_2$ blocking layer on indium tin oxide (ITO)-coated plastic substrates. The plasma approach offers several advantages compared to conventional thermal processes, in particular it enables the deposition of higher quality films, in terms of lower pinhole density, in the range of temperatures compatible with conductive plastic substrates.[28] This feature plays a key role to ensure high efficiency in the solid state devices. By incorporation of both the ALD-grown compact layer and the UV-irradiated scaffold in the fabrication process, and using a $CH_3NH_3PbI_{3-x}Cl_x$ perovskite layer, a doped 2,2′,7,7′-tetrakis-(N,N-di-p-methoxyphenylamine)9,9′-spirobifluorene (Spiro-O-MeTAD) as hole transport material (HTM), and a gold top contact, we obtain a PCE of 8.4% for a flexible plastic cell. This also represents the first example of low temperature and solution processed $TiO_2$ scaffold for perovskite solar cell either on glass or plastic. Furthermore, we developed a screen printable mesoporous formulation for the scaffold and patterning procedures compatible with the delicate plastic/ITO substrates (based on masking, laser definition and self-patterning) for the other layers enabling us to manufacture the first large-area (8 $cm^2$) integrated flexible perovskite photovoltaic module composed of 4 series-connected cells (PCE of 3.1% over the module and 4.3% over the its best cell).

F. Di Giacomo, S. Pescetelli, Dr. F. Matteocci, S. Razza, Prof. A. Di Carlo, Prof. T. M. Brown
Centre for Hybrid and Organic Solar Energy (CHOSE)
Department of Electronic Engineering
University of Rome – Tor Vergata
via del Politecnico 1, 00133 Rome, Italy
E-mail: thomas.brown@uniroma2.it

Dr. V. Zardetto, Prof. W. M. M. Kessels, Prof. M. Creatore
Department of Applied Physics
Eindhoven University of Technology
P. O. Box 513, 5600, MB, Eindhoven, The Netherlands

Dr. A. D'Epifanio, Prof. S. Licoccia
Department of Chemical Science and Technologies
University of Rome "Tor Vergata," Via della Ricerca Scientifica
00133 Rome, Italy

Dr. V. Zardetto, Prof. W. M. M. Kessels, Prof. M. Creatore
Solar Research Solliance
High Tech Campus 21, 5656, AE, Eindhoven, The Netherlands

**DOI: 10.1002/aenm.201401808**

  

ADVANCED ENERGY MATERIALS
www.advenergymat.de

Materials Views
www.MaterialsViews.com

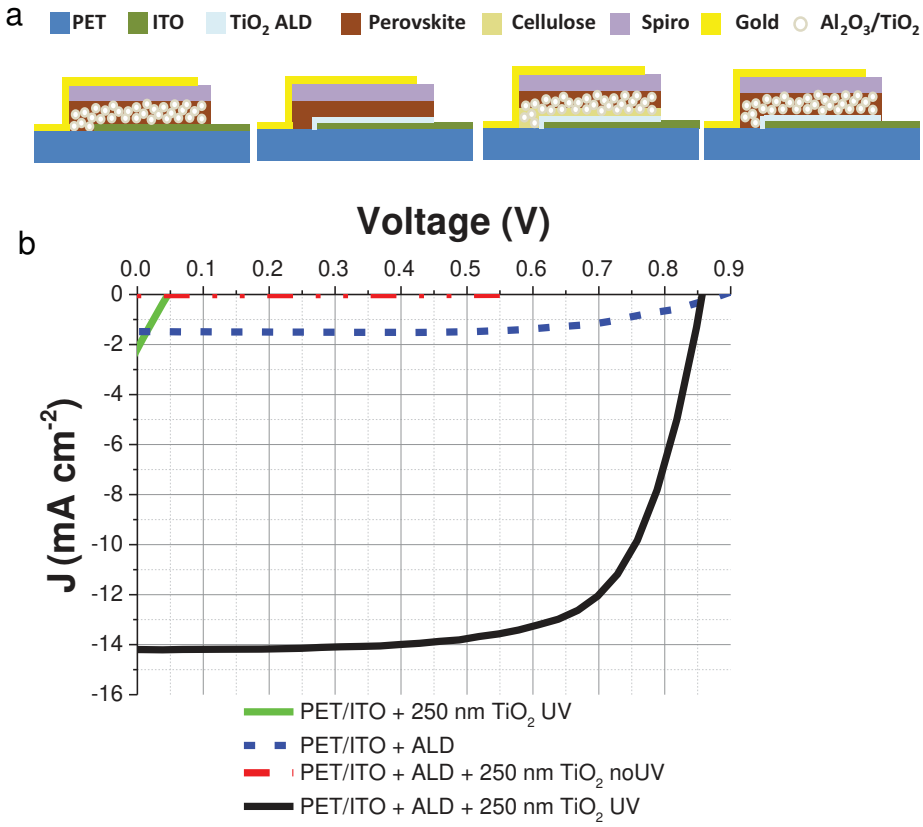


**Figure 1.** a) Cross-section schematics of the architecture we fabricated. From left to right: (1) cell with UV irradiated mesoporous $TiO_2$ electron extractor and no compact layer; (2) cell with ALD $TiO_2$ compact layer and without scaffold; (3) cell with ALD $TiO_2$ compact layer and mesoporous $TiO_2$ without UV irradiation; (4) cell with ALD $TiO_2$ compact layer and UV-irradiated mesoporous $TiO_2$. b) Current density–voltage curves of the best small area cells measured at 1 sun: light green continuous line is for a cell without ALD compact layer, blue dashed line for a cell with ALD compact layer and without scaffold, red dotted-dashed line for a cell with ALD compact layer and $TiO_2$ without UV irradiation, and black continuous line for a cell with ALD compact layer and UV irradiated $TiO_2$.

We fabricated a number of different flexible perovskite solar cells in the PET/ITO/ALD-$TiO_2$/(scaffold)/perovskite/Spiro-O-MeTAD/Au configuration, varying the scaffold (and its post-processing), with and without the compact ALD $TiO_2$ layer (**Figure 1**a). The *J*–*V* curves and photovoltaic parameters are shown in Figure 1b and **Table 1**. The first fabrication step consisted in the deposition of a compact layer of $TiO_2$ on the ITO/PET by ALD. This layer is crucial to avoid recombination of electrons in the ITO with holes in the perovskite semiconductor. Furthermore, we observed degradation phenomena occurring to the perovskite when it was deposited directly on the ITO without a compact layer (see Figure S1, Supporting Information) during prolonged annealing (>1.5 h at 95 °C). An initial thickness optimization was carried out on both planar and mesostructured architectures and the best results were obtained with an 11 nm thick ALD layer for both architectures.

The cell with an 11 nm-thick $TiO_2$ ALD compact layer and no scaffold exhibited a $V_{OC}$ of 870 mV. For these devices, the surface coverage of the perovskite layer was particularly high (see

**Table 1.** Photovoltaic parameters for the different types of architectures of $CH_3NH_3PbI_{(3-x)}Cl_x$ perovskite solar cells fabricated (all at the same time) on PET/ITO and glass/FTO. In the first four columns the substrate and the type of compact and scaffold layer used are specified. Cells are completed with Spiro-O-MeTAD as HTM and Au as contact. The average and the standard deviation (three cells for each architecture on PET and eight cells for glass) of the open circuit voltage ($V_{OC}$), short circuit current ($J_{SC}$), fill factor (FF), and power conversion efficiency (PCE) are reported. Parameters of the best cell are reported in brackets. In the last three columns the series resistance ($R_S$), shunt resistance ($R_{SH}$) and the time constant of the open circuit voltage decay measured for the best cell are also reported.

| Substrate [cm²] | Compact layer | Scaffold | $V_{OC}$ [mV] | $J_{SC}$ [mA cm$^{-2}$] | FF [%] | PCE [%] | $R_S$ [Ω cm²] | $R_{SH}$ [Ω cm²] | $\tau_2$ [ms] |
|---|---|---|---|---|---|---|---|---|---|
| PET ITO | ... | $TiO_2$ | 50 ± 20 (48) | −2.2 ± 0.9 (−2.2) | 14 ± 10 (17) | 0.01 ± 0.01 (0.018) | ... | ... | ... |
| PET ITO | $TiO_2$ ALD | ... | 870 ± 10 (879) | −1.2 ± 0.1 (−1.3) | 67 ± 7 (71) | 0.7 ± 0.1 (0.8) | 200 | 20000 | 1270 |
| PET ITO | $TiO_2$ ALD | $TiO_2$ UV | 826 ± 3 (828) | −12.3 ± 0.6 (−12.6) | 70 ± 1 (71) | 7.1 ± 0.3 (7.4) | 9.0 | 3300 | 500 |
| Glass FTO | ... | $TiO_2$ 450 °C | 670 ± 110 (790) | −4.0 ± 2.0 (−6.7) | 37 ± 9 (42) | 1.0 ± 0.9 (2.2) | 18.5 | 330 | 600 |
| Glass FTO | $TiO_2$ spray pyrolysis | ... | 930 ± 50 (938) | −11.0 ± 2.0 (−11.8) | 50 ± 8 (63) | 5.3 ± 1.3 (7.0) | 14.9 | 360 | 2340 |
| Glass FTO | $TiO_2$ spray pyrolysis | $TiO_2$ 450 °C | 806 ± 5 (802) | −17.1 ± 0.4 (−16.9) | 71 ± 2 (73) | 9.8 ± 0.1 (9.9) | 7.0 | 870 | 1590 |

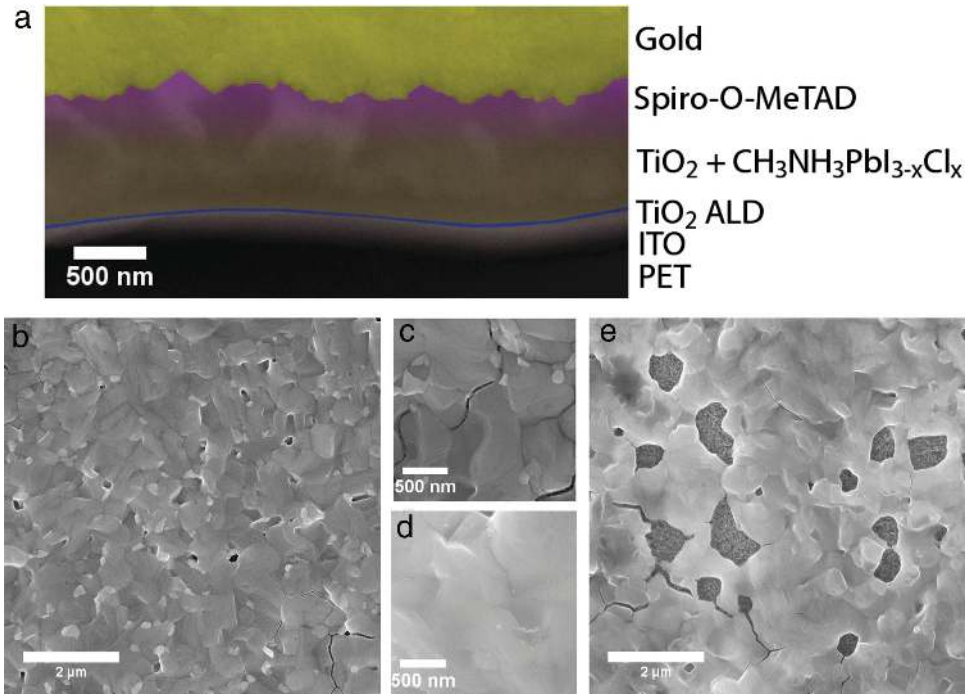


**Figure 2.** a) Colored cross-section SEM image of a plastic cell with ALD deposited $TiO_2$ compact layer and with UV irradiated mesoporous $TiO_2$. Colors are only rough guide the eye. b,c) Top view SEM image of $CH_3NH_3PbI_{3-x}Cl_x$ grown without scaffold on compact $TiO_2$ deposited by ALD on PET/ITO. d,e) Top view SEM image of $CH_3NH_3PbI_{3-x}Cl_x$ grown on UV irradiated $TiO_2$ scaffold on ALD-deposited compact $TiO_2$ on PET/ITO.

**Figure 2**b,c) with grain size of the order of hundreds of nanometers. The efficient hole blocking behavior of the ALD film is confirmed by the extremely low reverse current density in dark (0.004 mA $cm^{-2}$ at –1 V as shown in **Figure 3**). On the other hand, the forward current density in dark is also low, three orders of magnitude lower (0.015 mA $cm^{-2}$ at 1 V) than devices incorporating an UV-treated $TiO_2$ scaffold, and the series resistance, $R_S$ (200 Ω $cm^2$) is about one order of magnitude greater. The short current density (<1.5 mA $cm^{-2}$) and PCE (<1%) are in fact low for the scaffoldless devices on plastic being limited mainly by the ineffective charge injection in the ALD $TiO_2$ compact layer. This is confirmed by experiments carried out on scaffoldless devices on glass/FTO (see Figure S2, Supporting Information): unlike the cells with the $TiO_2$ compact layer made by spray pyrolysis where current densities were high, those fabricated with the ALD layer show low current densities similar to their plastic counterparts (even though the RMS surface roughness of FTO, 30 nm, is greater than ITO, 2.5 nm, which should even assist perovskite growth).[29] When we applied a mesoporous $Al_2O_3$ scaffold (generally used to facilitate the perovskite growth)[18] over the ALD compact layer, the $J_{SC}$ improved compared to the planar architecture (Figure S5, Supporting Information), but was still only 2.4 mA $cm^{-2}$. Forward current density curves in dark at 1 V was 3.5 mA $cm^{-2}$ indicate that the issues with injection have not been resolved with this type of non-injecting scaffold (as expected). In order to increase the efficiency of the devices, one can consider improving electron extraction via device interfacial engineering,[30] such as changing the ALD process parameters,[31] using interlayers on the compact layer such as $CsCO_3$, or PCBM,[32,33] or by introducing an electron-collecting $TiO_2$ scaffold layer. We adopted the latter strategy due to its additional benefits in driving the crystallization of the perovskite and improving device stability.[19]

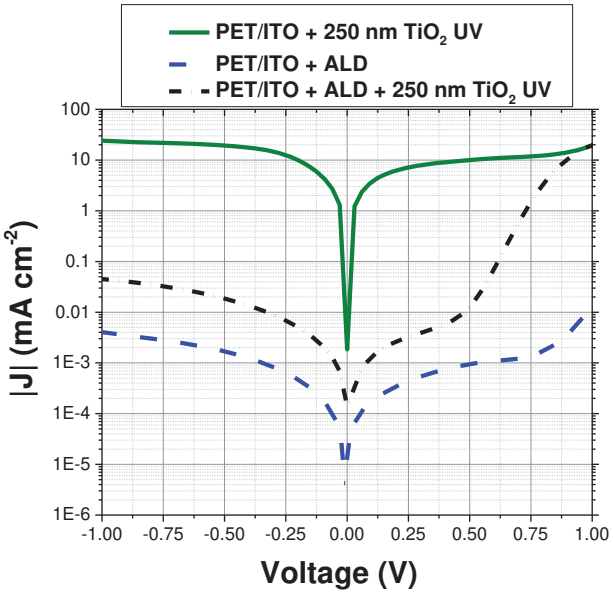


**Figure 3.** Tafel plot measured in dark. Green continuous line is for a cell without compact layer, blue dashed line for a cell with ALD compact layer without scaffold, and black dashed-dotted line for a cell with ALD compact layer and UV-irradiated $TiO_2$.

When a mesoporous $TiO_2$ scaffold was used, we observed different behaviors whether the layer was UV-processed or not. When incorporating the untreated $TiO_2$ film, devices exhibited

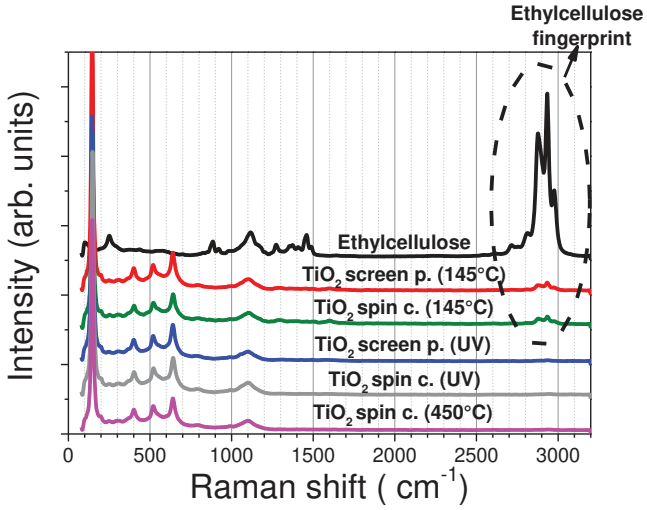


**Figure 4.** Raman spectra of different mesoporous $TiO_2$ highlighting the pure anatase phase of the $TiO_2$ and the cellulose binder removal with both UV irradiation and high temperature treatments.

an extremely low PCE of 0.001% (see Table 1) due to the lack of meaningful photocurrents (3 μA $cm^{-2}$), moderate $V_{OC}$ (550 mV), and also very high series resistance $R_S$ (33 000 Ω $cm^2$). The result is essentially related to the considerable presence of cellulose binder in the film (see Raman spectra in **Figure 4**). The permanence of the binder media can influence the perovskite growth at the interface with the scaffold, limit the contact surface between the perovskite and the mesoporous $TiO_2$, and block electron percolation toward the ITO due to the physical separation of the perovskite and the ITO. In fact, for the devices in which the 250 nm thick $TiO_2$ scaffold was UV-treated, the photovoltaic parameters increased dramatically yielding an average PCE of 7.1% (see Table 1) and a maximum PCE of 8.4% (see **Table 2**). Improved visible light transmittance, perovskite morphology, and electron injection in the $TiO_2$ underpin the enhancement of the PCE compared to the cells with no UV treatment and also with the $Al_2O_3$ scaffold. First, the substrate with the UV-treated $TiO_2$ layer exhibited the highest average light transmittance of the set (increasing to 84% from the value of 76% corresponding to the sample with the ALD layer only) due to its antireflection properties (see Figure S4, Supporting Information).[34] The perovskite layer covered most of the $TiO_2$ surface, in which emerging crystals can be identified and, although gaps are visible in the overlayer, it presents a more uniformly-connected morphology (see Figure 2d,e) with less defined grain boundaries with respect to the ones grown on the scaffoldless sample (see Figure 2b,c). Raman spectroscopy of the UV-treated and 450 °C-sintered $TiO_2$ layer shows that UV irradiation is very effective in removing cellulose binder (see Figure 4). The peaks relative to CH bonds in the ethylcellulose at 2876, 2934, 2976 $cm^{-1}$ disappear after 60 min of UV treatment due to cleavage of the cellulose chains (see Figure S5, Supporting Information).[35] $TiO_2$ is also in its anatase crystalline form (due to the presence of a peak at 144 $cm^{-1}$ and the absence of rutile peaks at 443 or 610 $cm^{-1}$) which is the preferred phase for its higher photocatalytical activity under UV irradiation.[36] The absorption spectrum of the UV-treated sample is also identical to the high temperature-treated glass sample (see Figure S4, Supporting Information) confirming complete binder removal. We have shown that $TiO_2$ particle interconnection is also improved via UV treatment leading to larger electron diffusion lengths in the layer.[23] In fact, the forward current density of the perovskite devices in dark becomes almost 20 mA $cm^{-2}$ at 1 V for the UV-treated 250nm-thick scaffold devices as shown in Figure 3, while the reverse current increases by one order of magnitude only, maintaining itself under 0.1 mA $cm^{-2}$. In addition $R_S$ decreases significantly from 33 000 to 9 Ω $cm^2$, which is close to that of glass-based devices processed at high temperatures (7 Ω $cm^2$). Together with an improved PCE the mesostructured device also delivered longer shelf-lifes with respect to the planar ones confirming the influence of scaffolds on stability as reported for glass based device in literature.[19] After keeping the unencapsulated devices in a dry box for a week, the scaffoldless cell lost 84% of its initial PCE while the mesoscopic cell lost only 8%.

It is the combination of the UV mesoporous scaffold and the high quality hole blocking compact layer on ITO-PET substrate that leads to the most efficient devices. The flexible solar cells with the UV treated $TiO_2$ scaffold but no PE-ALD $TiO_2$ layer exhibited poor efficiency (PCE = 0.01%) due to the extremely

**Table 2.** Photovoltaic parameters of PET/ITO/ALD-$TiO_2$/$TiO_2$ scaffold/perovskite/Spiro-O-MeTAD/Au devices. First two rows are small cells with scaffold deposition via spin coating and screen printing; 3rd row and 4th are for the large area perovskite solar cells and module made on PET/ITO with a screen printed scaffold. In the first two columns the active area size and the deposition technique of UV-irradiated $TiO_2$ scaffold are specified. In the following columns the average and the standard deviation (6 cells for small area) of the open circuit voltage ($V_{OC}$), short circuit current ($J_{SC}$), fill factor (FF), and power conversion efficiency (PCE) for cells obtained in a single batch are reported. Parameters of the best cell are reported in brackets. For the module, only the best device is reported. In the last three columns the series resistance ($R_S$), shunt resistance ($R_{SH}$) and the time constant of the open circuit voltage decay measured for the best cell are presented.

| Active area [$cm^2$] | $TiO_2$ scaffold deposition | $V_{OC}$ [mV] | $J_{SC}$ [mA $cm^{-2}$] | FF [%] | PCE [%] | $R_S$ [Ω $cm^2$] | $R_{SH}$ [Ω $cm^2$] | $\tau_2$ [ms] |
|---|---|---|---|---|---|---|---|---|
| 0.12 | Screen printing | 794 ± 8 (802) | −7.8 ± 0.4 (−7.8) | 68 ± 3 (70) | 4.2 ± 0.2 (4.4) | 12.4 | 4700 | 82 |
| 0.12 | Spin coating | 854 ± 6 (858) | −11.0 ± 3.0 (−14.1) | 68 ± 1 (70) | 6.2 ± 1.7 (8.4) | 7.2 | 3000 | 820 |
| 1.98 | Screen printing | 838 ± 11 (841) | −6.3 ± 1.3 (7.7) | 65 ± 3 (67) | 3.4 ± 0.7 (4.3) | 21.3 | 10 800 | ... |
| (Module) 7.92 | Screen printing | 3392 | −5.2 | 71 | 3.1 | 53 | 15 400 | ... |

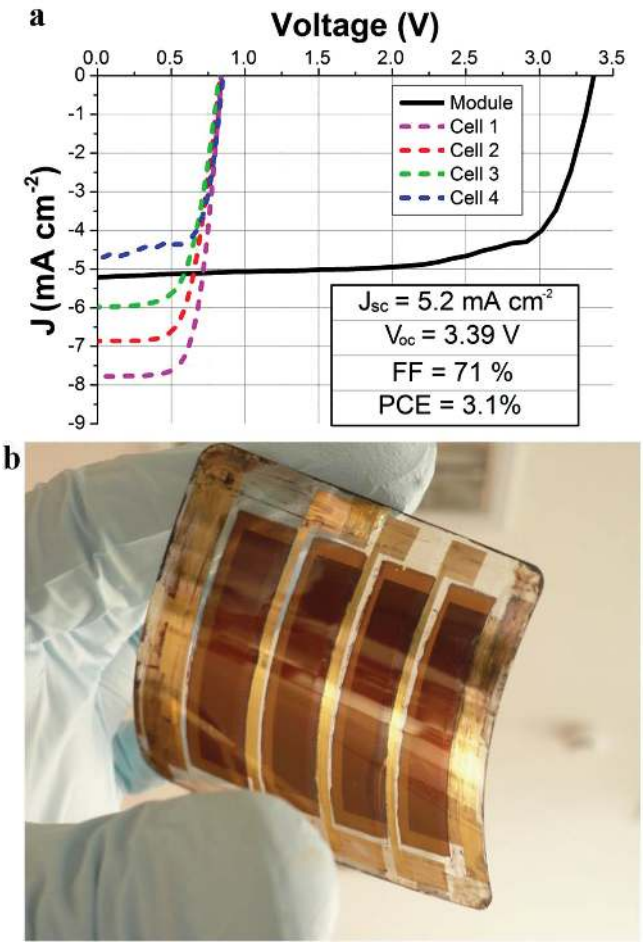


**Figure 5.** a) Current density–voltage plot of an integrated flexible module made of 4 series-interconnected cells based on $CH_3NH_3PbI_{(3-x)}Cl_x$ perovskite absorber with PET/ITO/ALD-$TiO_2$/$TiO_2$ scaffold/perovskite/Spiro-O-MeTAD/Au structure. Blue, green, red, and magenta dashed lines are relative to the single cells while the continuous black line is relative to the module. b) Picture of the 4 cell series-connected module (5.6 × 5.6 cm).

low $V_{OC}$ of 50 mV. In fact the absence of the compact $TiO_2$ layer led to very high recombination currents at the ITO/perovskite interface as revealed by the lack of diode-like behavior in the dark JV curves of Figure 3. The introduction of the 11 nm ALD $TiO_2$ compact layer brought rectifying behavior to the cell by reducing the back dark current by two–three orders of magnitude.

Transient voltage measurements enabled us to compare the different kinetics present in these devices. The transient decay in $V_{OC}$ showed a fast initial linear drop for all architectures, followed by a slower decay (see Figure S6, Supporting Information). The decay constants (inversely proportional to recombination rate) are listed in Table 1. More interestingly, since $V_{OC}$ is related to the population of excited electrons in the $TiO_2$, faster injection results in a rapid increase of $V_{OC}$ when exposing cells to light. Analysis of the $V_{OC}$ rise (see Figure S6, Supporting Information) does give an indication on the different injection kinetics obtained with the different layers. It is only the UV-treated $TiO_2$ in combination with the ALD compact layer that shows the same charging rate as that of a reference high-T mesostructured cell on glass, thus confirming its remarkable effectiveness when incorporated in plastic devices.

After developing the most efficient compact layer/scaffold combination at the cell level, we subsequently scaled up the process over large areas with the fabrication of a flexible photovoltaic module consisting of 4 series-connected cells on a 5.6 × 5.6 cm PET/ITO substrate (see picture in **Figure 5**).[37] For an efficient up-scaling, three key factors are mandatory: rational design of module interconnection,[38] homogenous deposition over large areas,[39] and precise pattering of the constituent layers.[40] In fact, in order to obtain efficient PV modules we had to develop effective patterning procedures, different from those carried out on glass/FTO, compatible with the delicate ITO/plastic substrates. These were carried out via a combination of protective masking films and laser patterning/cutting via a scanning $CO_2$ laser beam (see the Experimental Section and **Figure 6**) which enabled sufficiently high resolution and precise etching of the ITO, patterning of the compact layer (important since its presence would impede direct contact

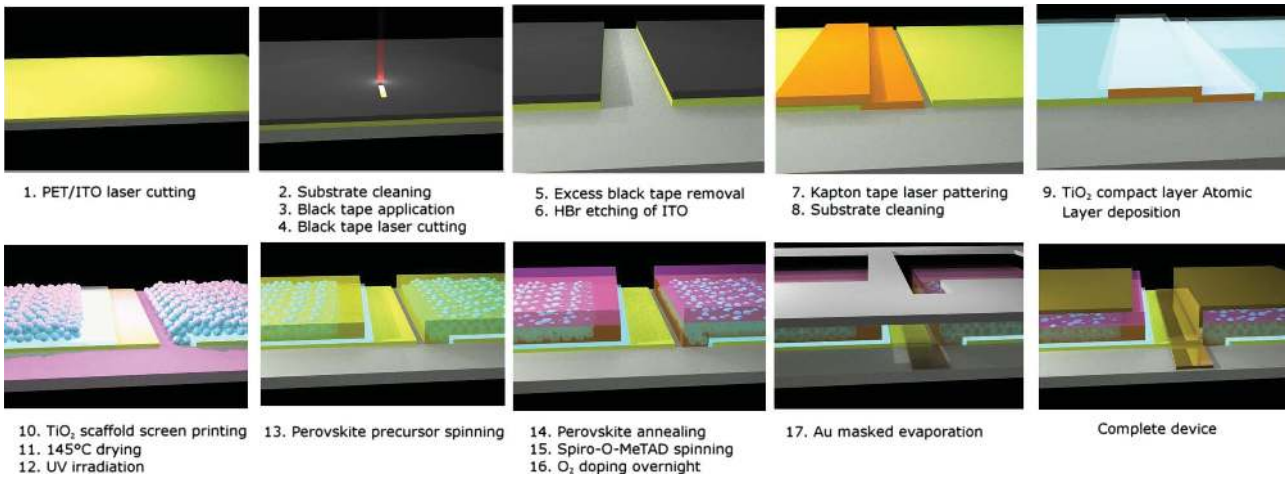


**Figure 6.** Schematics showing the module fabrication procedures divided in 17 steps.

between the gold and ITO series connections between cells leading to significantly lower fill factors)[40] and the definition of the shadow mask used for evaporation of the Au contact, so as to avoid short circuit with the ITO pad of the same cell. For the remaining mesoporous $TiO_2$, perovskite and HTM layers, a careful manual removal was performed using a tip dipped in a DMF/chlorobenzene solution. In future, this can be replaced by developing automated and higher resolution selective laser ablation processes with ultra-fast pulses for plastics (starting from those already successfully implemented on glass devices).[40,41]

Spin coating was used for the perovskite and HTM layers since we found these to be transferable over the module size. Initially, we also spin coated the $TiO_2$ but the post-removal to define the cell stripes of all three layers was problematic leading to shunting between the cells and/or higher resistance on the interconnection areas after the top contact evaporation. Resulting modules had low PCEs below 0.7%. A remarkable improvement was achieved by developing formulations via the much more suitable technique for large-area coating of the mesoporous $TiO_2$, i.e., screen printing. In fact, the $TiO_2$/UV-treatment combination we developed allows one to maintain binders in the $TiO_2$ paste formulation which can thus be easily and uniformly deposited over large areas with this technique, problematic if attempted with binder-free pastes.[10] The tailored screen-printable formulation (see the Experimental Section), which crucially enables the direct deposition of a patterned scaffold (in its final rectangular shape), was analyzed with Raman spectroscopy, showing effective removal of binders after UV irradiation, similarly to its spin-coatable counterpart (see Figure 3 and Figure S5, Supporting Information). We found that keeping the ITO surface between the cells of the modules bare prior to perovskite and HTM deposition, thanks to the patterned $TiO_2$ scaffolds, also greatly assisted the patterning of the two overlayers. In fact, we observed that the contact angle of the perovskite solution was much higher on the ITO (60°) compared to the $TiO_2$ (23°). A similar trend was measured for chlorobenzene too (34° for ITO and 14° for $TiO_2$). The gradient in contact angle between the ITO and the $TiO_2$ (both planar and mesoscopic) drives away the perovskite and the HTM solution from the bare ITO interconnection area during the spin coating process (see Figure S7, Supporting Information), allowing for a degree of self-patterning of these layers. This effect led to a much less demanding and easy post-patterning/cleaning procedure, and thus more reproducible modules with high fill factors of over 70%.

Consequently, the module with the patterned ALD layer (via the laser defined masking procedure) and the UV-treated screen-printed patterned $TiO_2$ outperformed the spin-coated equivalent over large areas yielding a PCE of 3.1%, a fill factor of 71%, a $V_{OC}$ of 3.4 V and a $J_{SC}$ of 5.2 mA cm$^{-2}$ (see Figure 5a), together with a lower $R_S$ (53 vs 189 Ω cm$^2$) and an higher $R_{SH}$ (15 600 vs 6540 Ω cm$^2$). Note that no hysteresis was detected during the PV measurements of modules (see last panel of Figure S8, Supporting Information). The layout we designed allowed us to also measure the individual cells of the module in order to study uniformity and reproducibility of the fabrication process. By increasing the active area from 0.12 cm$^2$ (single test cells) to 1.98 cm$^2$ (unit cells of the module) the average efficiency with the same materials/processes showed a moderate 19% relative drop, from 4.2% to 3.4%. The best large-area cell of the module delivered a PCE of 4.3%. Due to the partial manual definition of the cell patterns and the uniformity of deposition of the active layers via spin coating on non-perfectly planar substrates, variability amongst the cells affected the PCE of the module. The module's performance was limited by the least efficient cell on the substrate as result of the series connection.[38]

Higher efficiencies are achievable considering that further development of the screen printable pastes should bring performance in line with devices with the more often utilized spin-coated scaffold, which led us to obtain 8.4%. The different paste compositions (solvent mix and dilution) and deposition techniques (as well as the evaporation rates) influence the $TiO_2$ morphology and consequently the internal interface between $TiO_2$ and perovskite and the growth of the latter. The spin coated cells exhibit an average PCE 48% higher than the screen printed ones (see Table 2). Since devices with screen printed scaffolds possess a lower $V_{OC}$ and open circuit voltage decay time constant (one order of magnitude) compared to that with the spin-coated scaffold (see Table 2) it appears that the performance is limited by recombination processes. Thus, there is scope to develop even more effective UV-processable screen-printable pastes in the future together with more automated patterned deposition of the perovskite and HTM layers to approach the efficiencies also seen on glass.

Finally, to validate the PET/ITO/ALD_$TiO_2$_CL/UV_treated_$TiO_2$ scaffold/perovskite/HTM/Au materials and device design, the PV characterization was complemented by an investigation on its mechanical resistance to bending. Flexibility is an important functionality which adds appeal to a PV technology developed on plastic substrates.[10,42] **Figure 7** shows how the cell successfully maintains all of its initial PCE after a sequence of 100 bending cycles at 30, 20, and 15 mm radii of curvature in succession (300 cycles overall). In fact, Zardetto et al. showed that 14 mm represents the limit for safe bending radius of PET/ITO (variations can be expected between different suppliers).[9]

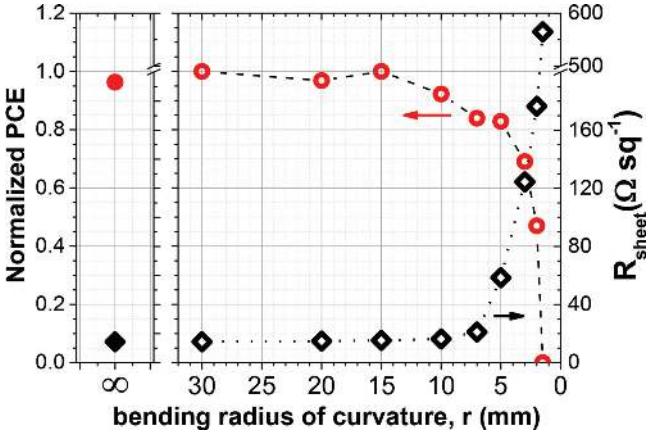


**Figure 7.** Effect of bending tests on the PCE of a PET/ITO/ALD-$TiO_2$/$TiO_2$ scaffold/perovskite/Spiro-O-MeTAD/Au solar cell (circles) and on the sheet resistance of bare ITO/PET substrates (diamonds). Filled symbols are relative to sample measured before any bending. The samples were conformed to a cylinder with known radius 100 times (50 on each side) to study the effect of both compression and extension stress and were measured flat after these bending procedures.

Each 100 cycles were the succession of 50 compression + 50 tensile bending cycles since it is known that the two stresses give rise to differing degradation rates.[9] At smaller radii the PCE significantly degrades, mainly due to increase in the sheet resistance (see Figure 7) which is related to formation of cracks in the brittle ITO.[9] These in turn can damage the active layers over the ITO leading to a significant increase in the recombination current and a decrease in the injection forward current (see Figure S9, Supporting Information) all contributing in lowering PV performance. However, it is important to note that the complete device is mechanical resistant to bending down to the 15 mm radius scale at least and likely even more if a less brittle transparent conducting bottom contact can be found.

In summary, the first examples of flexible perovskite photovoltaic modules were fabricated. A new type of low temperature processed $TiO_2$ scaffold was successfully applied to fabricate efficient flexible solar cell devices. By using UV irradiation to remove organic binders and promote interparticle bonding, together with a low temperature plasma assisted ALD compact layer, the best flexible plastic solar cells we fabricated exhibited an efficiency of 8.4%, significantly higher than devices without compact layer or scaffold (and more durable than these). The formulation of a screen printable $TiO_2$ paste, together with the definition of the ALD compact layers via masking/laser patterning procedures, was instrumental in fabricating a flexible perovskite module with a power conversion efficiency of 3.1% on plastic substrates, with the best cell of the module presenting a PCE of 4.3%. The main materials, architecture and processes (solution processing, screen printing, ALD, laser patterning, UV-irradiation) developed are also potentially transferable to roll-to-roll processing.[43,44] Mechanical flexibility of the device was excellent and any degradation of PV performance below the ≈1 cm scale in curvature of bending cycles was mainly ascribed to brittle ITO degradation. Routes for achieving further performance enhancements involve improving cell-to-cell uniformity, the formulation of optimized screen printable pastes and the automation of the deposition and patterning processes.

Note: Just days before the second submission of this paper, an article on flexible scaffoldless single cells with ALD compact layers was published.[49] Our results, here published, demonstrate not only the first ever flexible perovskite cells with scaffold but also flexible perovskite photovoltaic modules.

## Experimental Section

To create the desired electrodes pattern, PET/ITO substrates (Flexvue, 15 Ω $\square^{-1}$, 26 × 26 mm cut with $CO_2$ laser, surface roughness (RMS) = 2, 5 nm) were etched with an HBr solution masking with laser-cut black tape. Patterned substrates were cleaned by 10 min of ultrasonic bath, using ethanol. The compact $TiO_2$ film was deposited onto the ITO surface by atomic layer deposition (ALD) technique. The layers on small and large area were prepared in a remote plasma reactor (FlexAL™) with the substrate temperature held at 150 °C. A preplasma treatment (200 W) of 3 min was performed prior to the ALD deposition. The pressures were maintained in the range of 10–80 mTorr during all the deposition, while the base pressure of the reactor was ≈$10^{-5}$ Torr. A single ALD cycle consists in (i) 2*s* Ti(CpMe)$(NMe_2)_3$ precursor dosing, (ii) 5*s* $O_2$ plasma exposure (200 W), with these steps separated by purging steps of 2*s* with argon flow. 190 cycles were repeated in order to achieve the desired thickness of 11 nm. For spin coating on plastic a customized vacuum chuck was used to keep the substrate flat. The mesostructured scaffold was deposited by spin coating or screen printing. For $Al_2O_3$ a commercial dispersion (Sigma Aldrich 702129) was diluted in isopropyl alcohol (IPA) 1:2 weigh ratio and spin coated at 2000 rpm to obtain a thickness of 250 nm. For $TiO_2$ a commercial paste (Dyesol 18-NRT) was diluted in ethanol with 1:5 weigh ratio and spin coated at 1500 rpm to obtain the same thickness. For screen printing on plastic, the commercial paste was diluted with terpineol. The resulting paste showed a low viscosity if compared to the one used for glass substrate, since no other binders were added to avoid incomplete photo-oxidation. This formulation gives better results (2-fold increase respect to the paste used for glass/FTO) when processed with UV irradiation on plastic.

The final thickness of the scaffold was measured via profilometer (Dektak Veeco 150). All scaffolds were annealed in a closed hot plate at 140 °C for 30 min. $TiO_2$ mesoporous scaffold underwent an UV irradiation with an estimated power density of 225 mW $cm^{-2}$ (Dymax EC 5000 UV lamp with a metal-halide bulb PN38560 Dymax that contains no UV-C) for 1 h.

FTO/glass substrates (Pilkington, 8 Ω $\square^{-1}$, 25 × 25 mm, surface roughness (RMS) = 30 nm) were etched via raster scanning laser (Nd:$YVO_4$ pulsed at 30 kHz average output power $P$ = 10 W). Patterned substrates were cleaned by ultrasonic bath, first using glass detergent, than acetone and finally IPA. A compact $TiO_2$ film was deposited onto the FTO surface by spray pyrolysis deposition (SPD) technique using a previously reported procedure.[27] Onto the substrates with the $TiO_2$ compact a thin film of $TiO_2$ nanoparticles based paste (18NR-T Dyesol diluted with terpineol, ethylcellulose, isopropanol, and ethanol) was screen-printed and successively sintered at 480 °C for 30 min.[45]

Methylammonium iodide was synthetized following a previously reported procedure,[6] while $PbCl_2$ (Aldrich, 98%) was used as received. Before perovskite deposition all plastic substrate underwent 10 min of UV irradiation for a further cleaning, since ALD film were used weeks after fabrication. The perovskite was deposited by spin-coating (2000 rpm for 60 s) from a dimethylformamide solution of methylammonium iodide and $PbCl_2$ (3:1 molar ratio) in Nitrogen atmosphere, followed by 15 min drying at room temperature. The perovskite is formed after heating at 95 °C for 90 min followed by a rapid annealing at 120 °C for 10 min.

The hole-transporting material (HTM) was deposited by spin coating a solution of 2,20,7,70-tetrakis-(N,N-dip-methoxyphenylamine)9,9′-spirobifluorene (Spiro-O-MeTAD) at 2000 rpm for 60 s in nitrogen atmosphere and left in air overnight in a closed dry box. The solution was prepared adding 75 mg of Spiro-O-MeTAD (Lumtec), 8 µL of 4-tert-butylpyridine and 14.2 µL of a 520 mg $mL^{-1}$ $LiN(CF_3SO_2)_2N$ solution in acetonitrile to 1 mL of chlorobenzene.[46]

Small area cells were cleaned on the edges with a chlorobenzene-DMF blend (7:1 volume ratio). The same solution was used to clean the interconnection between cells on the module using a ruler and an empty marker.

Samples were introduced into a high vacuum chamber ($10^{-6}$ mbar) in order to evaporate Au back contacts (thickness 80 nm) by thermal evaporation. An evaporation mask defined a devices area of 0.16 $cm^2$ for small area cells. For modules a layout made with 4 series-connected cells of 1.98 $cm^2$ active area each was used. The layout allowed to measure single cell and module.

Masked devices (0.12 $cm^2$ aperture for small area device) were tested under a Class A solar simulator (ABET Sun 2000) at AM1.5 and 100 mW $cm^{-2}$ illumination conditions calibrated with a reference Silicon cell (RERA Solutions RR-1002), using a Keithley 2420 as a source-meter in ambient condition without sealing. Sun simulator spectrum and class were measured with a BLACK-Comet UV-VIS Spectrometer. No mask has been used to measure the module after checking that the active area (here equal to intersection between gold and ITO) was well defined. For single cell measure the other cell were masked. *IV* measurement presented in the main text refers to the reverse scan (from $V_{OC}$ to $J_{SC}$). High hysteresis effect were measured for planar and $Al_2O_3$ based cells (up to 50%), whereas $TiO_2$ based cells showed a much more limited effect (up to 15%) as already reported in literature.[47] Extended data of hysteresis effect on all architecture are reported in Figure S8, Supporting Information.

Open circuit voltage decay was measured using the mechanical shutter of the ABET Sun 2000 sun simulator, recording the $V_{OC}$ with a Tektronics TDS1001B oscilloscope. The decay shows for all architectures a fast initial linear drop, followed by a slower decay. Since the first part was similar for all devices and can be hardly resolved by the experimental setup, the discharge was fitted with an exponential decay starting from the end of the linear decay, obtaining a $R^2$ bigger than 0.98 in all cases. Dark *JV* curves were measured using a Keithley 2420 as a source meter with the devices stored in a black box.

For the bending resistance test, the cell was bended 600 times on a cylinder with known radius. Every 50 cycles the cell was flipped to experience both compression and extension stresses and every 100 cycles an *IV* measure was taken. After the *IV* measure a smaller cylinder was used. The set of used radii was: 30, 20, 15, 10, 7 and 5, 3, 2, and 1.5 mm. For the bending test a cell with UV-irradiated $TiO_2$ scaffold was used while a bare PET/ITO substrate was used to measure the effect on the sheet resistance.

Scanning electron microscopy images were measured with a FE-SEM Leo Supra 35. For cross-section image the sample was left in liquid nitrogen for 30 s and then cut with a scissor, so the constituent layers are not perfectly defined.

Raman spectroscopy was conducted through Jobin-Yvon-Horiba micro-Raman system (LabRAM ARAMIS) equipped with Ar+ ion laser (514 nm) as excitation source (100 mW). The Horiba micro-spectrometer is coupled with a confocal microscope that allows the spatial resolution of the sample through detector pinhole aperture. The cut-off from the notch filters in the spectrometer is less than 120 $cm^{-1}$. The spectrometer is equipped with a diffraction grating of 1800 lines/mm coupled to a CCD camera. The laser light reached the sample surface at normal incidence by means of 100× objective. The scattered radiation was collected in a backscattering geometry. Spectral deconvolution was carried out by nonlinear least-squares fitting of the Raman peaks to a mixture of Lorentzian and Gaussian line shapes, providing the peak position of each Raman band. Spectra were smoothed with a FFT filter (cut-off frequency = 0.08).

For contact angle measurements, a 5 µL drop of the desired solution was slowly put on the substrate with a micropipette. Then a picture of the drop profile was taken with a digital camera and analyzed with ImageJ using the low-bond axisymmetric drop shape analysis plug-in.[48] All measurements were taken at 20 °C and approximately 50% of relative humidity.

## Supporting Information

Supporting Information is available from the Wiley Online Library or from the author.

## Acknowledgements

F.D.G. and V.Z. contributed equally to this work. Thanks are due to Ms. C. D'Ottavi, Mr. A. L. Palma, and Mr. A. Di Ludovico for their valuable technical support. The authors acknowledge "Polo Solare Organico" Regione Lazio the "DSSCX" MIUR-PRIN2010, the "AQUASOL" PRIN 2012 (2012A4Z2RY) project, and ENERGY.2012.10.2.1 (NANOMATCELL, Grant Agreement No. 308997) for funding. The research of M.C. has been funded by the Netherlands Organization for Scientific Research (NWO, Aspasia program).

Received: October 12, 2014
Published online:

[1] A. Kojima, K. Teshima, Y. Shirai, T. Miyasaka, *J. Am. Chem. Soc.* **2009**, *131*, 6050.
[2] N. G. Park, *J. Phys. Chem. Lett.* **2013**, *4*, 2423.
[3] H. S. Kim, C. R. Lee, J. H. Im, K. B. Lee, T. Moehl, A. Marchioro, S. J. Moon, R. Humphry-Baker, J. H. Yum, J. E. Moser, M. Gratzel, N. G. Park, *Sci. Rep.* **2012**, *2*, 591.
[4] NREL, http://www.nrel.gov/ncpv/images/efficiency_chart.jpg, (accessed **2014**).
[5] K. Wojciechowski, M. Saliba, T. Leijtens, A. Abate, H. J. Snaith, *Energy Environ. Sci.* **2014**, *7*, 1142.
[6] J. Burschka, N. Pellet, S. J. Moon, R. Humphry-Baker, P. Gao, M. K. Nazeeruddin, M. Grätzel, *Nature* **2013**, *499*, 316.
[7] D. Liu, T. L. Kelly, *Nat. Photonics* **2014**, *8*, 133.
[8] M. Saliba, K. W. Tan, H. Sai, D. T. Moore, T. Scott, W. Zhang, L. A. Estroff, U. Wiesner, H. J. Snaith, *J. Phys. Chem. C* **2014**,*118* ,17171 .
[9] V. Zardetto, T. M. Brown, A. Reale, A. Di Carlo, *J. Polym. Sci., Part B: Polym. Phys.* **2011**, *49*, 638.
[10] T. M. Brown, F. De Rossi, F. Di Giacomo, G. Mincuzzi, V. Zardetto, A. Reale, A. Di Carlo, *J. Mater. Chem. A* **2014**, *2*, 10788.
[11] N. S. Lewis, *Science* **2007**, *315*, 798.
[12] V. Zardetto, G. Mincuzzi, F. De Rossi, F. Di Giacomo, A. Reale, A. Di Carlo, T. M. Brown, *Appl. Energy* **2014**, *113*, 1155.
[13] P. Docampo, J. M. Ball, M. Darwich, G. E. Eperon, H. J. Snaith, *Nat. Commun.* **2013**, *4*, 2761.
[14] J. You, Z. Hong, Y. M. Yang, Q. Chen, M. Cai, T. B. Song, C. C. Chen, S. Lu, Y. Liu, H. Zhou, Y. Yang, *ACS Nano* **2014**, *8*, 1674.
[15] C. Roldan-Carmona, O. Malinkiewicz, A. Soriano, G. Minguez Espallargas, A. Garcia, P. Reinecke, T. Kroyer, M. I. Dar, M. K. Nazeeruddin, H. J. Bolink, *Energy Environ. Sci.* **2014**, *7*, 994.
[16] M. H. Kumar, N. Yantara, S. Dharani, M. Graetzel, S. Mhaisalkar, P. P. Boix, N. Mathews, *Chem. Commun.* **2013**, *49*, 11089.
[17] N. J. Jeon, H. G. Lee, Y. C. Kim, J. Seo, J. H. Noh, J. Lee, S. I. Seok, *J. Am. Chem. Soc.* **2014**, *136*, 7837.
[18] T. Leijtens, G. E. Eperon, S. Pathak, A. Abate, M. M. Lee, H. J. Snaith, *Nat. Commun.* **2013**, *4*, 2885.
[19] C. Law, L. Miseikis, S. Dimitrov, P. Shakya-Tuladhar, X. Li, P. R. F. Barnes, J. Durrant, B. C. O'Regan, *Adv. Mater.* **2014**, *26*, 6268.
[20] A. Mei, X. Li, L. Liu, Z. Ku, T. Liu, Y. Rong, M. Xu, M. Hu, J. Chen, Y. Yang, M. Grätzel, H. Han, *Science* **2014**, *345*, 295.
[21] J. M. Ball, M. M. Lee, A. Hey, H. J. Snaith, *Energy Environ. Sci.* **2013**, *6*, 1739.
[22] V. Zardetto, G. De Angelis, L. Vesce, V. Caratto, C. Mazzuca, J. Gasiorowski, A. Reale, A. Di Carlo, T. M. Brown, *Nanotechnology* **2013**, *24*, 255401.
[23] V. Zardetto, F. Di Giacomo, D. Garcia-Alonso, W. Keuning, M. Creatore, C. Mazzuca, A. Reale, A. Di Carlo, T. M. Brown, *Adv. Energy Mater.* **2013**, *3*, 1292.
[24] G. Dingemans, W. M. M. Kessels, *J. Vacuum Sci. Technol., A* **2012**, *30*, 040802.
[25] A. K. Chandiran, A. Yella, M. T. Mayer, P. Gao, M. K. Nazeeruddin, M. Grätzel, *Adv. Mater.* **2014**, *26*, 4309.
[26] Y. Wu, X. Yang, H. Chen, K. Zhang, C. Qin, J. Liu, W. Peng, A. Islam, E. Bi, F. Ye, *Appl. Phys. Express* **2014**, *7*, 052301.
[27] D. Garcia-Alonso, V. Zardetto, A. J. M. Mackus, F. De Rossi, M. A. Verheijen, T. M. Brown, W. M. M. Kessels, M. Creatore, *Adv. Energy Mater.* **2014**, *4*, 1300831.
[28] H. B. Profijt, S. E. Potts, M. C. M. van de Sanden, W. M. M. Kessels, *J. Vacuum Sci. Technol., A* **2011**, *29*, 050801.
[29] G. E. Eperon, V. M. Burlakov, P. Docampo, A. Goriely, H. J. Snaith, *Adv. Funct. Mater.* **2014**, *24*, 151.
[30] H. Zhou, Q. Chen, G. Li, S. Luo, T.-b. Song, H.-S. Duan, Z. Hong, J. You, Y. Liu, Y. Yang, *Science* **2014**, *345*, 542.
[31] A. Paracchino, N. Mathews, T. Hisatomi, M. Stefik, S. D. Tilley, M. Gratzel, *Energy Environ. Sci.* **2012**, *5*, 8673.
[32] J. Kim, G. Kim, T. K. Kim, S. Kwon, H. Back, J. Lee, S. H. Lee, H. Kang, K. Lee, *J. Mater. Chem. A* **2014**, *2*, 17291.

[33] L. Qin, Z. Xie, L. Yao, Y. Yan, S. Pang, F. Wei, G. G. Qin, *Phys. Status Solidi RRL* **2014**, *9999*, 912.
[34] B. Richards, *Sol. Energy Mater. Sol. Cells* **2003**, *79*, 369.
[35] H. Fan, G. Li, F. Yang, L. Yang, S. Zhang, *J. Chem. Technol. Biotechnol.* **2011**, *86*, 1107.
[36] T. Luttrell, S. Halpegamage, J. Tao, A. Kramer, E. Sutter, M. Batzill, *Sci. Rep.* **2014**, *4*, 4043.
[37] F. Matteocci, S. Razza, F. Di Giacomo, S. Casaluci, G. Mincuzzi, T. M. Brown, A. D'Epifanio, S. Licoccia, A. Di Carlo, *Phys. Chem. Chem. Phys.* **2014**, *16*, 3918.
[38] F. Giordano, E. Petrolati, T. M. Brown, A. Reale, A. Di Carlo, *IEEE Trans. Electron Devices* **2011**, *58*, 2759.
[39] S. Razza, F. Di Giacomo, F. Matteocci, L. Cinà, A. L. Palma, S. Casaluci, P. Cameron, A. D'Epifanio, S. Licoccia, A. Reale, T. M. Brown, A. Di Carlo, *J. Power Sources* **2015**, *277*, 286.
[40] F. Matteocci, L. Cinà, F. Di Giacomo, S. Razza, A. L. Palma, A. Guidobaldi, A. D'Epifanio, S. Licoccia, T. M. Brown, A. Reale, A. Di Carlo, *Prog. Photovoltaics: Res. Appl.* **2014**, DOI: 10.1002/pip.2557.
[41] G. Mincuzzi, L. Vesce, M. Schulz-Ruhtenberg, E. Gehlen, A. Reale, A. Di Carlo, T. M. Brown, *Adv. Energy Mater.* **2014**, *4*.
[42] A. Fakharuddin, R. Jose, T. M. Brown, F. Fabregat-Santiago, J. Bisquert, *Energy Environ. Sci.* **2014**, *7*, 3952.
[43] P. Poodt, A. Lankhorst, F. Roozeboom, K. Spee, D. Maas, A. Vermeer, *Adv. Mater.* **2010**, *22*, 3564.
[44] F. C. Krebs, *Sol. Energy Mater. Sol. Cells* **2009**, *93*, 465.
[45] F. Di Giacomo, S. Razza, F. Matteocci, A. D'Epifanio, S. Licoccia, T. M. Brown, A. Di Carlo, *J. Power Sources* **2014**, *251*, 152.
[46] H. Li, K. Fu, P. P. Boix, L. H. Wong, A. Hagfeldt, M. Grätzel, S. G. Mhaisalkar, A. C. Grimsdale, *ChemSusChem* **2014**, *7*, 3420.
[47] H. J. Snaith, A. Abate, J. M. Ball, G. E. Eperon, T. Leijtens, N. K. Noel, S. D. Stranks, J. T.-W. Wang, K. Wojciechowski, W. Zhang, *J. Phys. Chem. Lett.* **2014**, *5*, 1511.
[48] A. F. Stalder, T. Melchior, M. Müller, D. Sage, T. Blu, M. Unser, *Colloids Surf., A* **2010**, *364*, 72.
[49] B.-J. Kim, D. H. Kim, Y.-Y. Lee, H.-W. Shin, G. S. Han, J. S. Hong, K. Mahmood, T. Ahn, Y.-C. Joo, K. S. Hong, N.-G. Park, S. Lee, H. S. Jung, *Energy Environ. Sci.* **2014**.